RZ 3928 (# ZUR1803-054) 03/22/2018
Physics 9 pages

Research Report

Monolithically integrated InGaAs microdisk lasers on silicon using template-assisted selective epitaxy

S. Mauthe, B. Mayer, M. Sousa, G. Villares, P. Staudinger, H. Schmid, K. Moselund

IBM Research – Zurich
8803 Rüschlikon
Switzerland

This is the author prepared version of the article published by SPIE:
S. Mauthe, B. Mayer, M. Sousa, G. Villares, P. Staudinger, H. Schmid, K. Moselund
"Monolithically integrated InGaAs microdisk lasers on silicon using template-assisted selective epitaxy"
Proc. SPIE 10672, Nanophotonics VII, 106722U (4 May 2018); doi: 10.1117/12.2306640;
https://doi.org/10.1117/12.2306640

Copyright 2018 Society of Photo-Optical Instrumentation Engineers (SPIE). One print or electronic copy may be made for personal use only. Systematic reproduction and distribution, duplication of any material in this paper for a fee or for commercial purposes, or modification of the content of the paper are prohibited.

LIMITED DISTRIBUTION NOTICE

This report has been submitted for publication outside of IBM and will probably be copyrighted if accepted for publication. It has been issued as a Research Report for early dissemination of its contents. In view of the transfer of copyright to the outside publisher, its distribution outside of IBM prior to publication should be limited to peer communications and specific requests. After outside publication, requests should be filled only by reprints or legally obtained copies (e.g., payment of royalties). Some reports are available at http://domino.watson.ibm.com/library/Cyberdig.nsf/home.

Research
Africa • Almaden • Austin • Australia • Brazil • China • Haifa • India • Ireland • Tokyo • Watson • Zurich

Monolithically integrated InGaAs microdisk lasers on silicon using template-assisted selective epitaxy

S. Mauthe[a], B. Mayer[a], M. Sousa[a], G. Villares[a], P. Staudinger[a], H. Schmid[a], and K. Moselund[a]

[a]IBM Research – Zurich, Säumerstr. 4, 8803 Rüschlikon, Switzerland

ABSTRACT

As performance and power consumption of modern micro-chips are increasingly limited by electrical on-chip interconnects, all-optical interconnect systems promise data transmission at speed of light and wavelength-division multiplexing. To realize complex networks, active devices, like lasers, need to be integrated on Si. III-Vs are excellent candidates for optical devices, however, their integration on Si is challenging due to a significant lattice and thermal mismatch. Template-assisted selective epitaxy (TASE) was recently developed by our group, allowing for the selective growth of III-Vs from a small Si seed in a confined oxide template. In this work, we extend TASE towards optical devices and demonstrate the monolithic integration of InGaAs lasers via a novel approach using a virtual substrate (VS) in a two-step templated growth. First, μm^2 sized 60 nm thick InGaAs VSs are grown by MOCVD using TASE on SOI. Subsequently, 500 nm oxide are deposited onto the VS and patterned in arbitrary shapes like disks, and rings. In a second InGaAs growth, the defined vertical cavities are filled. The investigated structures have diameters of $\sim 1.7\,\mu m$, thicknesses of $0.5\,\mu m$ and total cavity volumes of $0.5\,\lambda_0^3$. Photoluminescence spectroscopy reveals a broad spontaneous emission peak around $1.1\,\mu m$ (FWHM = 150 nm) that increases linearly with pump power for low excitation powers ($<< 2.6$ pJ/pulse). Above excitation threshold, a strong emission peak emerges at $1.1\,\mu m$ (FWHM = 7 nm). The Input-Output curve (log-log, $T = 10\,K$) exhibits the characteristic S-shape which constitutes a strong indication for the lasing operation. The onset of the lasing threshold is observed up to 200 K with a characteristic temperature of $T_0 = 192\,K$.

Keywords: Semiconductor laser, microdisk, monolithic integration, III-V epitaxy, silicon photonics, InGaAs, MOCVD

1. INTRODUCTION

In the past, the density of integrated circuits on electrical chips has increased due to a tremendous decrease in size of electrical components. Along with downscaling of electronic devices the chip complexity increased resulting in longer interconnect paths.[1] In electrical interconnects the charged nature of electrons leads to coulomb interactions and crosstalk between electronic information, limiting the data range transmitted through the interconnect.[2] Moreover, the rising power consumption of electronics limits the overall chip performance and the interconnects rather than the active electronic devices are responsible for an increasing fraction of energy consumed. Consequently, a novel interconnect concept is required to further enhance the performance of on-chip data communication. One possibility to replace resistive metal lines and hence, overcome the interconnect bottleneck, is an all-optical interconnect system promising data transmission at the ultimate speed limit of light and allowing wavelength-division multiplexing.[3,4] The consequent drive to replace electronic components by optical devices has become a key driver of semiconductor and nano research during the past decade.[5] On the way towards all optical networks, efficient passive devices such as waveguides,[6] as well as, active devices like, modulators,[7] and photodetectors,[8] have been demonstrated on Si. The electro-optical light source however, has mostly been employed off-chip since efficient sources, likes lasers, are yet to be integrated seamlessly on Si.[9]

III-Vs are excellent candidates for efficient lasers due to their direct tunable bandgap and high electron mobility. The integration of high quality III-V on Si however, poses an essential challenge since Si and III-Vs exhibit a significant lattice and thermal mismatch. In order to overcome this challenge, several techniques, like

Further author information: (Send correspondence to S. Mauthe)
S. Mauthe: E-mail: svm@zurich.ibm.com, Telephone: +41 44 724 8044

wafer bonding, buffered layer growth,[10,11] masked growth,[12,13]and nanowire growth,[14,15] have been developed allowing for the integration of III-V lasers on Si.

Another promising approach, called template-assisted selective epitaxy (TASE),[16,17] has recently been developed to integrate nanoelectronic devices on Si.[18,19] TASE allows for the selective growth of III-V materials from a small Si seed in a confined oxide template and hence, the integration of high quality III-V material on Si in arbitrary shapes. Recently, we extended TASE towards optical devices and demonstrated the monolithic integration of GaAs lasers on Si using a direct cavity approach. GaAs disk lasers of only $0.5\,\lambda_0^3$ were fabricated and showed lasing around 835 nm at room temperature.[20]

For on-chip applications however, it is desirable to work above the absorption edge of silicon at $1.1\,\mu$m in order to use Si for passives. In this work, we extend TASE towards optical devices and demonstrate the monolithic integration of InGaAs lasers (with an indium content around 40 %) on Si via a novel approach using a virtual substrate in a two-step templated growth process.

2. METHODS

2.1 Monolithic Integration of III-V on Si

2.1.1 Virtual Substrate Approach

In this work, we extend TASE to the integration of optical devices on Si via a novel approach using a virtual substrate (VS) in a two-step templated growth process (see Figure 1). For further details on the TASE process please refer to references 16 and 17. An SOI wafer with $2\,\mu$m buried oxide (BOX) is used providing a high refractive index contrast between the optical III-V device and the bottom Si substrate and serves as an optical isolation for the lasing mode. In a first step, the top 60 nm Si layer are patterned to define the expansion of the virtual substrate using e-beam lithography and inductively coupled plasma (ICP) etch. Next, a 200 nm silicon oxide shell is deposited using atomic layer deposition (ALD) and plasma-enhanced chemical vapor deposition (PECVD TEOS). This oxide layer serves as a template for the growth of the virtual substrate and defines its geometry. Subsequently, reactive ion etching (RIE) is used to dry etch openings into the oxide template and reveal the underlying patterned Si layer (see 2. in Figure 1). Using TMAH (tetramethylammonium hydroxide) wet etch, the Si layer is partly etched in a controlled way until a small Si part is left serving as a seed area ($100 \times 60\,\text{nm}^2$) for the subsequent InGaAs nucleation. Next, $\text{In}_x\text{Ga}_{1-x}\text{As}$ is grown using metalorganic chemical vapor deposition (MOCVD). The targeted composition is $x = 30\,\%$, however, using TASE, any desired composition can be achieved, since there is no requirement for lattice matching. The InGaAs selectively grows from the Si seed into the predefined oxide template. The composition of the InGaAs is defined by the growth parameters: temperature, V-III ratio, and precursor flows (see values in Table 1). The obtained InGaAs structures have a thickness of 60 nm and a size of $\sim 1\,\mu\text{m}^2$ (defined by the template geometry and growth duration). This will serve as a virtual substrate for the growth of the optical device.

After the growth of the InGaAs virtual substrate, a thick silicon oxide layer (500 nm) is deposited using PECVD. The oxide layer is patterned and an opening is etched down to the virtual substrate using an RIE

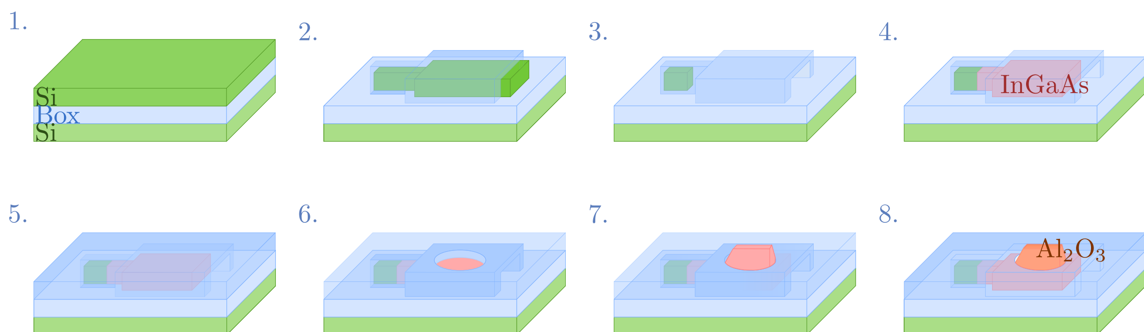

Figure 1: Template-assisted selective epitaxy (TASE) process flow (see details in reference 16 and 17. Growth of virtual substrate in step 4, growth of resonator gain material in step 7.

Table 1: MOCVD growth parameters employed during the virtual substrate and gain material growth (see steps 4 and 7 in Figure 1).

Growth Step	Temperature [°C]	V/III Ratio	TMIn Flow [μmol/min]	TMGa Flow [μmol/min]	TBA Flow [μmol/min]
Virtual Substrate	560	32	68.8	1.66	299
Gain Material	560	32	68.8	1.66	299

dry etch and a final BHF etch. Arbitrary shapes, such as rings, disks, and wires, can be patterned, acting as a template for the second growth and confining it in lateral direction. In a second growth step, InGaAs is grown from the virtual substrate using MOCVD. In a first attempt, the growth parameters are kept constant compared to the growth of the virtual substrate, in order to achieve a similar $In_xGa_{1-x}As$ composition (see Table 1).

Finally, a thin Al_2O_3 layer is deposited using ALD to passivate exposed surfaces.

2.1.2 Structural Analysis

The fabricated structures are analyzed using scanning electron microscopy (SEM), scanning transmission electron microscopy (STEM), and energy-dispersive X-ray spectroscopy (EDS). Using Ga focused-ion beam etching (FIB), a lamella is prepared at operating voltages of 30 kV and 5 kV for final polishing. The STEM and EDS characterizations were performed using a double spherical aberration corrected JEOL ARM200F microscope operated at 200 kV.

Figure 2 shows the top view of ring and disk structures imaged using SEM after the second MOCVD growth. For all structures, ring and disk resonators, the growth is confined by the predefined template and does not exceed it. The outer diameter of the ring and the first disk structure measures $\sim 1.7\,\mu$m; the inner diameter of the ring $\sim 0.6\,\mu$m. The second disk structure (Figure 2c) exhibits by design a smaller diameter of $\sim 1.2\,\mu$m. The SEM analysis reveals a polycrystalline material structure for the ring and first disk structure. The second disk structure reveals a less polycrystalline shape, however, defect lines are also present. All devices shown in Figure 2 are optically characterized and show similar behavior. A detailed optical characterization of the devices is given in Section 3.

In order to further investigate the crystal quality of the structures, STEM and EDS spectroscopy is performed on the disk structure in Figure 2b. A cross-section is obtained along the dashed line indicated in Figure 2b. Figure 3 shows an overview of the cavity in the center, as well as, four high resolution bright field (BF) STEM images at marked positions. The cross-section confirms the polycrystalline structure of the grown InGaAs material and reveals several defects and grain boundaries (darker lines in Figure 3). From this low resolution image the initial nucleation at the Si is visible, as well as, the virtual substrate (lower, darker 60 nm thick region).

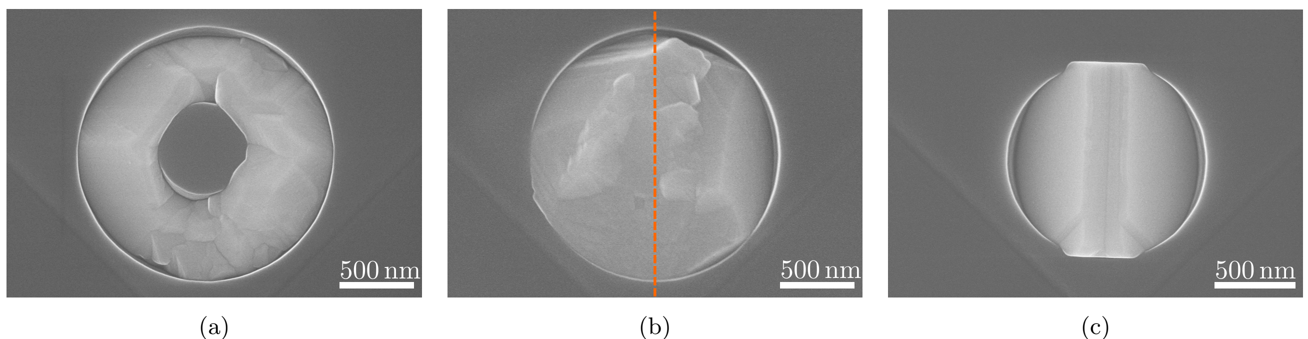

(a) (b) (c)

Figure 2: Top view SEM images of (a) ring, (b) disk 1, and (c) disk 2 resonators. Dashed line in (b) corresponds to the location of the FIB lamella cut.

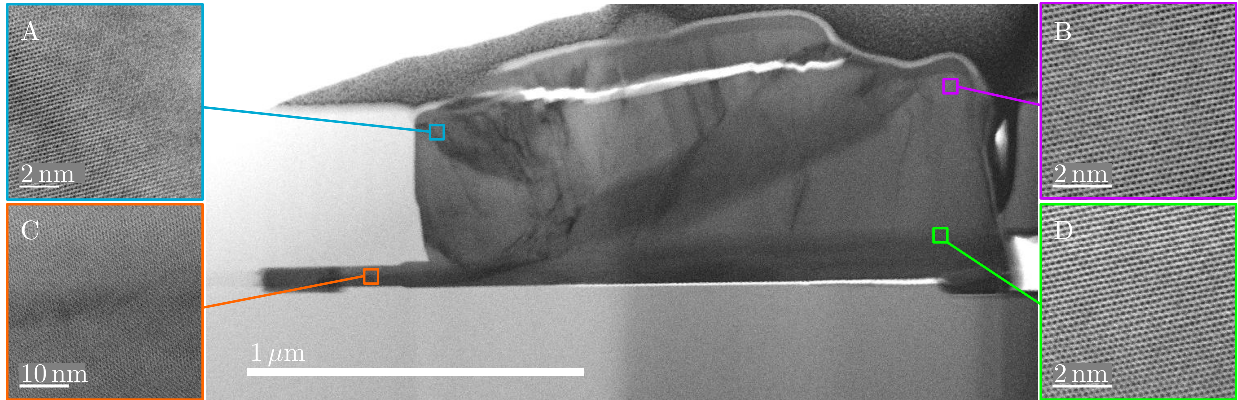

Figure 3: STEM image of the disk structure at the marked position in Figure 2b (dashed line). The center image shows an overview of the structure. Four high resolution images are taken at the marked positions.

Table 2: EDS material analysis performed on the locations marked in Figure 3. An average area of 8 nm^2 is analyzed. The analysis is performed using DigitalMicrograph, Version 3.12.1200.0, Gatan Inc.

Location	Indium [%]	Gallium [%]
A	44	56
B	47	53
C	37	63
D	34	66

Using EDS, chemical maps are acquired for the four high resolution images in Figure 3. The material analysis is performed with DigitalMicrograph software from Gatan Inc. The arsenic content is assumed to be constant, indium and gallium contents are simulated with the software analysis tool. The results are listed in Table 2 and represent the composition x of the $\text{In}_x\text{Ga}_{1-x}\text{As}$. We could observe a small variation of $\sim 3\,\%$ between left and right, however, this variation is within the error of the simulation of $\pm 3\,\%$. Moreover, a clear change in indium composition throughout the structure in vertical direction is evident. The lower part of the structure, namely the virtual substrate, exhibits an indium content of $\sim 36\,\%$, the upper part, the actual growth of the disk, exhibits $\sim 46\,\%$. This difference in indium content is a result of individual precursor diffusion during the two independent growth steps (see step 4 and 7 in Figure 1). During MOCVD growth, precursors are transported via two mechanisms: diffusion in vapor and surface diffusion.[21] Therefore, the growth is influenced by the material and shape of the template, as well as, the size of the opening towards the area of nucleation. Having a look at the two individual growth steps during the presented fabrication, the first growth is determined by a diffusion into a several μm long oxide template with an opening of 60 nm $\times$ 3600 nm. The second growth on the other hand, is determined by a diffusion into a wide opened ($d = 1.7\,\mu$m) oxide template with a height of only 500 nm. The differences in geometry and surface result in a different transport of the precursors to the nucleation area and hence, a difference in composition. Generally, it would be possible to compensate this geometrical dependence by an appropriate change in precursor flows.

The identified different InGaAs compositions of the virtual substrate and the disk growth result in a lattice mismatch of 0.04 Å. This is expected to lead to strain and the subsequent formation of defects. Defects are clearly visible in the provided SEM and STEM images (Figure 2 and 3).

2.2 Optical Characterization

Fabricated samples have been optically examined using a micro-photoluminescence setup (depicted in Figure 4). The setup consists of a pulsed supercontinuum laser (78 MHz, NKT Photonics SuperK Extreme), a cryostat allowing the sample to be cooled down to ~ 4 K (CryoVac), a spectrometer (grating 830 g/mm, blaze 1.2 μm), and an InGaAs photo detector (Princeton Instruments PyLoN-IR).

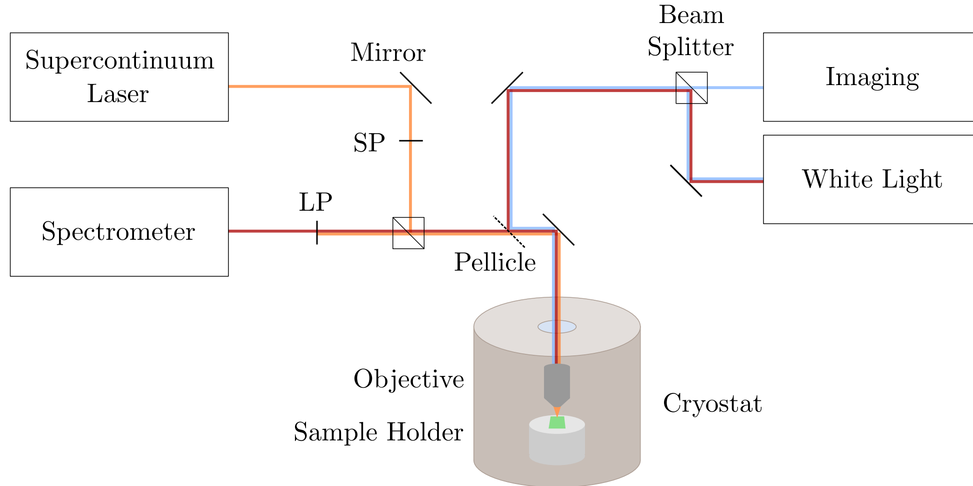

Figure 4: Sketch of the micro-PL setup used for optical characterization. The three main parts are a supercontinuum laser, a cryostat with the sample, and a spectrometer with a detector.

The samples are optically pumped using the pulsed supercontinuum laser at 830 nm. Before impinging on the sample, the excitation beam passes a 900 nm shortpass filter to filter out higher order diffractions of the supercontinuum laser. Optionally, a chopper wheel can be inserted into the beam path allowing only 2.5 % of the excitation laser to pass protecting small structures from the detrimental effects of excessive heating.

A 50x objective (NA = 0.45) focuses the excitation beam onto the sample. The objective is mounted inside the cryostat, in working distance of the samples. The samples are mounted in the cryostat and cooled down to $\sim 4\,\mathrm{K}$. Throughout the measurement, the samples are heated in steps of $10\,\mathrm{K} - 50\,\mathrm{K}$ up to room temperature. Photoluminescence spectroscopy is performed at each temperature point.

The photoluminescent response of the sample is collected from the top through the objective. A 900 nm longpass filter is used to block the excitation laser to the spectrometer. The collected light impinges on the spectrometer and via a grating onto an InGaAs detector.

To quantify the input power of the excitation laser at 830 nm, a power meter was used to measure the excitation power. The power was measured after the excitation beam passes the objective and before impinging on the sample. Hence, the optical losses due to the quartz glass opening of the cryostat, and the objective were taken into account. Using this measured intensity and the repetition rate of the laser, the threshold values provided in this work are in pJ/pulse.

A white light source can be added to the beam path using a removable pellicle allowing to image the samples.

3. EXPERIMENTAL RESULTS

Photoluminescence spectroscopy was performed on all fabricated devices in Figure 2. The devices were optically pumped using a supercontinuum laser at 830 nm. All devices, show a broad spontaneous emission background for low excitation powers ($<< 2.4$ pJ/pulse) at low temperature ($T < 10\,\mathrm{K}$). The spontaneous emission peaks are centered around 1115 nm (FWHM=150 nm) and increase linearly with increasing pump power for low excitation powers (sub threshold). This measured FWHM is rather broad for spontaneous emission at low temperature due to the identified change in composition throughout the structure (see Section 2.1.2).

At pulsed excitation powers above 2.4 pJ/pulse, the ring resonator shows a strong emission peak emerging at 1145 nm from the clamped spontaneous emission background. A second, less strong emission peak, arises at 1218 nm. Figure 5a shows the photoluminescence spectrum of the ring resonator (blue) at an excitation power of ≈ 2.4 pJ/pulse. With further increasing the excitation power ($>> 2.4$ pJ/pulse), the emission peak strongly increases non-linearly and finally reaches a lasing regime (see Figure 6a). The peak position slightly shifts with increasing excitation energy towards lower wavelengths. The Input-Output curve of the strong emission peak at 1145 nm of the ring laser is shown in Figure 5b. The log scale reveals a characteristic S-shape which

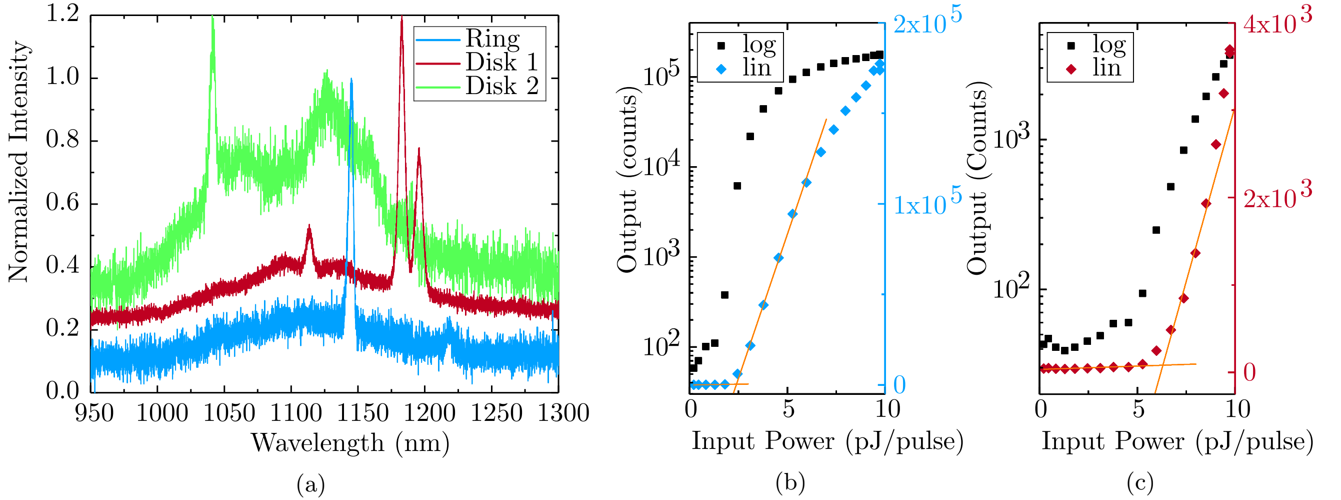

(a) (b) (c)

Figure 5: (a) Normalized photoluminescence spectrum of ring (blue), disk 1 (red), and disk 2 (green) resonator at low excitation powers (~ 2.4 pJ/pulse, ~ 6.3 pJ/pulse, and ~ 5.1 pJ/pulse respectively). Note that for better visualization, the red and green plot were shifted by 0.2. Measurement performed at low temperatures $T < 10$ K. Input-Output curve of (b) ring and (c) disk 1.

constitutes a strong indication for the lasing operation of the device at $T = 10$ K. In linear scale a clear kink is visible depicting the onset of the lasing peak at 2.4 pJ/pulse.

The FWHM reduces clearly from 148 nm to 3.5 nm around the threshold power of 2.4 pJ/pulse. With further increasing excitation powers ($>> 2.4$ pJ/pulse), the FWHM interestingly, slightly increases again to FWHM = 10 nm. One possible explanation for this deviation from the characteristic Shawlow-Townes limit might be related to a variation of the real refractive index n with carrier density N, namely the linewidth enhancement factor α.[22,23] It has been demonstrated that semiconductors, such as GaAs,[24] InAs,[25] and $In_{0.53}Ga_{0.47}As$,[26] exhibit a change in refractive index depending on the carrier density dn/dN. The magnitude of the change dn/dN is material dependent. Moreover, the presented devices exhibit a complex material structure with varying indium content throughout the resonator structure and hence, varying refractive indexes.[27] We believe since the linewidth enhancement factor might be different for individual compositions that these changes in composition also impact the linewidth of the strong emission peaks.

The first disk resonator (Figure 2b) exhibits two strong emission peaks at excitation powers of 6.3 pJ/pulse. Both peaks increase non-linearly with increasing excitation powers. The Input-Output curve of the strong emission peak at 1198 nm is plotted in Figure 5c. Again, a characteristic S-shape curve is revealed in the log scale and a clear kink is visible in the linear scale constituting a strong indication for the lasing operation of the device at $T = 5$ K. The spectrum of the second disk laser (Figure 2c) reveals a single strong emission peak at 1040 nm with a threshold of 5.1 pJ/pulse.

To further quantify the devices, the lasing performance was investigated at different temperatures. Starting at low temperature ($T = 10$ K), the sample was heated in steps of 10 K up to room temperature and the photoluminescence response of the individual devices measured. Figure 6b shows the strong emission peak of the ring resonator at different temperatures. The intensity of the strong emission peak decreases with increasing temperature. Around $T = 100$ K the peak position shifts by ~ 4 nm. The threshold onset of the strong emission peak at different temperatures is plotted in Figure 6c. A characteristic temperature of $T_0 = 192$ K can be extracted using the empirical relation $I_{th} = I_0 \exp(T/T_0)$. This characteristic temperature compares to values achieved in III-V quantum dot disk laser.[10,28]

A more detailed analysis of the data in Figure 6c, reveals a kink at ~ 100 K along with the identified wavelength shift in Figure 6b. Similar observations have been reported before and attributed to carrier loss mechanisms.[29] In reference 29, Sanchez at al. observed several kinks in the characteristic temperature and identified carrier leakage across a heterobarrier to be the most important carrier loss mechanism. In our work,

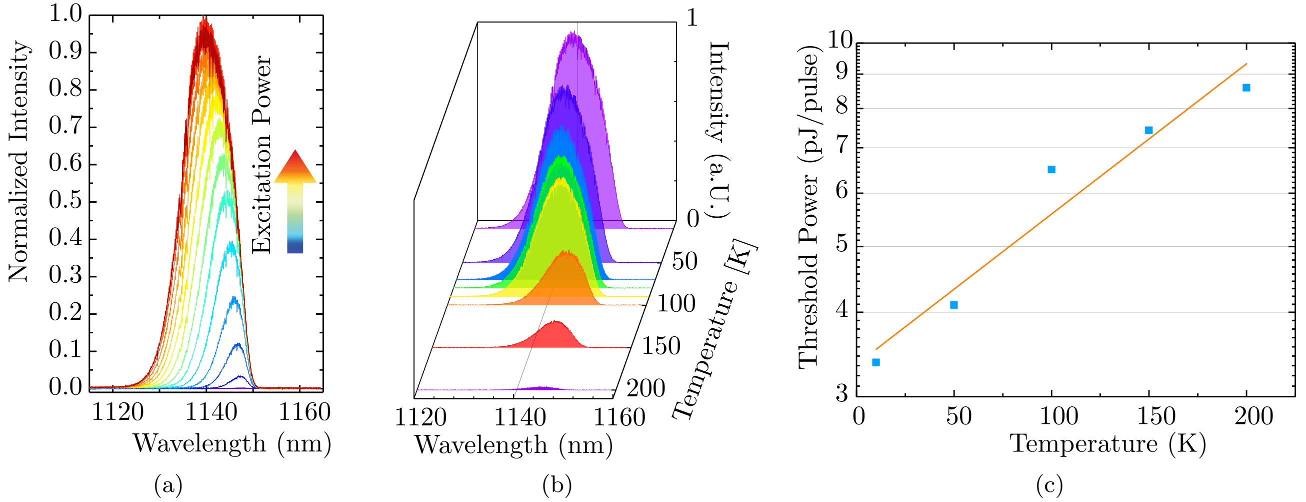

Figure 6: (a) Ring cavity strong emission peak for increasing excitation powers. (b) Normalized spectrum of the strong emission peak from the ring resonator at different temperatures. (c) Threshold power plotted at different temperatures. The orange line resembles the fit to determine the characteristic temperature T_0 (fit performed in ln scale, data plotted in log scale).

no intentional barriers are present, however, due to the identified polycrystalline structure, heterobarriers are unintentionally present. Therefore, the observed kink and wavelength shift might be associated with carrier leakage over heterobarriers.

4. CONCLUSION

In summary, we demonstrated the monolithic integration of InGaAs microring and -disk lasers on Si using TASE growth in a virtual approach. The measured devices showed characteristic S-shaped Input-Output curves and exhibited threshold excitation powers as low as 2.4 pJ/pulse at temperatures up to 200 K (ring). Compared to previous work, we extended the virtual substrate approach towards the ternary alloy InGaAs and hence, achieved emission at energies smaller than the Si bandgap. The latter is an advantage when working with integrated silicon photonics, where we would like to exploit Si for the passive devices.

A detailed material analysis was performed using SEM, STEM, and EDS. SEM and STEM revealed a polycrystalline structure. Moreover, EDS spectroscopy identified a composition change throughout the structure with varying indium composition ranging from about 34 % to 47 %. Despite the presence of defects and grain boundaries, the measured devices showed evidence for lasing.

Due to geometry and growth characteristics, the virtual substrate exhibited a different composition than the gain material. However, by careful optimization of growth conditions it should be possible to compensate these effects in future work. Furthermore, since the presented fabrication process is suitable for any III-V material, a binary virtual substrate, such as InP, could be grown reducing the complexity and allowing for the growth of lattice matched $In_{0.53}Ga_{0.47}As$.

Temperature dependent measurements showed lasing behavior up to 200 K and characteristic temperature of $T_0 = 192$ K. The characteristic temperature is comparable to values achieved in III-V QD laser.

In conclusion, the presented work shows the potential of TASE and the virtual substrate approach to directly integrate InGaAs micro cavity emitters on Si.

ACKNOWLEDGMENTS

We received financial support from H2020 ERC project PLASMIC, Grant #678567. We acknowledge J. Winiger, L. Czornomaz, Y. Baumgartner, M. Tschudy, and J. Leuthold for technical discussions and assistance.

REFERENCES

[1] Miller, D. A. B., "Optical interconnects to electronic chips," *Appl. Opt.* **49**, F59–F70 (Sep 2010).

[2] Miller, D. A. and Ozaktas, H. M., "Limit to the bit-rate capacity of electrical interconnects from the aspect ratio of the system architecture," *Journal of Parallel and Distributed Computing* **41**(1), 42–52 (1997).

[3] Mishra, S., Chaudhary, N. K., and Singh, K., "Overview of optical interconnect technology," *International Journal of Scientific & Engineering Research* **3**(4) (2012).

[4] Miller, D. A. B., "Device Requirement for Optical Interconnects to Silicon Chips," *Proc. of IEEE Special Issue on Silicon Photonics* **97**(7), 1166–1185 (2009).

[5] ITRS - Executive Summary, "ITRS - Executive Summary," *IEEE Comput* (2007).

[6] Xia, F., Sekaric, L., and Vlasov, Y., "Ultracompact optical buffers on a silicon chip," *Nature Photonics* **1**(1), 65–71 (2007).

[7] Xu, Q., Schmidt, B., Pradhan, S., and Lipson, M., "Micrometre-scale silicon electro-optic modulator," *Nature* **435**(7040), 325–327 (2005).

[8] Assefa, S., Xia, F., and Vlasov, Y. A., "Reinventing germanium avalanche photodetector for nanophotonic on-chip optical interconnects," *Nature* **464**(7285), 80–84 (2010).

[9] Sun, C., Wade, M. T., Lee, Y., Orcutt, J. S., Alloatti, L., Georgas, M. S., Waterman, A. S., Shainline, J. M., Avizienis, R. R., Lin, S., Moss, B. R., Kumar, R., Pavanello, F., Atabaki, A. H., Cook, H. M., Ou, A. J., Leu, J. C., Chen, Y.-H., Asanovi, K., Ram, R. J., Popovi, M. A., and Stojanovi, V. M., "Single-chip microprocessor that communicates directly using light," *Nature* **528**, 534–538 (Dec. 2015).

[10] Shi, B., Zhu, S., Li, Q., Tang, C. W., Wan, Y., Hu, E. L., and Lau, K. M., "1.55 <i>μ</i> m room-temperature lasing from subwavelength quantum-dot microdisks directly grown on (001) Si," *Applied Physics Letters* **110**(12), 121109 (2017).

[11] Li, Q., Wan, Y., Liu, A. Y., Gossard, A. C., Bowers, J. E., Hu, E. L., and Lau, K. M., "1.3um inas quantum-dot micro-disk lasers on v-groove patterned and unpatterned (001) silicon," *Opt. Express* **24**, 21038–21045 (Sep 2016).

[12] Kim, H., Farrell, A. C., Senanayake, P., Lee, W. J., and Huffaker, D. L., "Monolithically Integrated InGaAs Nanowires on 3D Structured Silicon-on-Insulator as a New Platform for Full Optical Links," *Nano Letters* **16**(3), 1833–1839 (2016).

[13] Shi, Y., Wang, Z., Campenhout, J. V., Pantouvaki, M., Guo, W., Kunert, B., and Thourhout, D. V., "Optical pumped ingaas/gaas nano-ridge laser epitaxially grown on a standard 300-mm si wafer," *Optica* **4**, 1468–1473 (Dec 2017).

[14] Lu, F., Bhattacharya, I., Sun, H., Tran, T.-T. D., Ng, K. W., Malheiros-Silveira, G. N., and Chang-Hasnain, C., "Nanopillar quantum well lasers directly grown on silicon and emitting at silicon-transparent wavelengths," *Optica* **4**, 717–723 (Jul 2017).

[15] Mayer, B., Janker, L., Loitsch, B., Treu, J., Kostenbader, T., Lichtmannecker, S., Reichert, T., Morkötter, S., Kaniber, M., Abstreiter, G., Gies, C., Koblmüller, G., and Finley, J. J., "Monolithically Integrated High-β Nanowire Lasers on Silicon," *Nano Letters* **16**(1), 152–156 (2016).

[16] Schmid, H., Borg, M., Moselund, K., Gignac, L., Breslin, C. M., Bruley, J., Cutaia, D., and Riel, H., "Template-assisted selective epitaxy of iii-v nanoscale devices for co-planar heterogeneous integration with si," *Applied Physics Letters* **106**(23) (2015).

[17] Czornomaz, L., Uccelli, E., Sousa, M., Deshpande, V., Djara, V., Caimi, D., Rossell, M. D., Erni, R., and Fompeyrine, J., "Confined epitaxial lateral overgrowth (celo): A novel concept for scalable integration of cmos-compatible ingaas-on-insulator mosfets on large-area si substrates," in [*2015 Symposium on VLSI Technology (VLSI Technology)*], T172–T173 (June 2015).

[18] Convertino, C., Cutaia, D., Schmid, H., Bologna, N., Paletti, P., Ionescu, A. M., Riel, H., and Moselund, K. E., "Investigation of inas/gasb tunnel diodes on soi," in [*2017 Joint International EUROSOI Workshop and International Conference on Ultimate Integration on Silicon (EUROSOI-ULIS)*], 148–151 (April 2017).

[19] Borg, M., Schmid, H., Moselund, K. E., Signorello, G., Gignac, L., Bruley, J., Breslin, C., Das Kanungo, P., Werner, P., and Riel, H., "Vertical iiiv nanowire device integration on si(100)," *Nano Letters* **14**(4), 1914–1920 (2014). PMID: 24628529.

[20] Wirths, S., Mayer, B., Schmid, H., Lörtscher, E., Sousa, M., Riel, H., and Moselund, K., "Room Temperature Lasing from Monolithically Integrated GaAs Microdisks on Si," *CLEO/Europe-EQEC* (2017).

[21] Borg, M., Schmid, H., Moselund, K. E., Cutaia, D., and Riel, H., "Mechanisms of template-assisted selective epitaxy of InAs nanowires on Si," *Journal of Applied Physics* **117**(14) (2015).

[22] Henry, C. H., "Theory of the Linewidth of Semiconductor Lasers," *IEEE Journal of Quantum Electronics* **18**(2), 259–264 (1982).

[23] Koblmüller, G., Mayer, B., Stettner, T., Abstreiter, G., and Finley, J. J., "GaAs AlGaAs core shell nanowire lasers on silicon : invited review," *Semicond. Sci. Technol.* **32**, 1–22 (2017).

[24] Mendoza-Alvarez, J. G., Nunes, F. D., and Patel, N. B., "Refractive index dependence on free carriers for GaAs," *Journal of Applied Physics* **51**(8), 4365–4367 (1980).

[25] Yu, Z. G., Krishnamurthy, S., and Guha, S., "Photoexcited-carrier-induced refractive index change in small bandgap semiconductors," *Journal of the Optical Society of America B* **23**(11), 2356 (2006).

[26] Gozu, S., Mozume, T., and Ishikawa, H., "Refractive index study of n-type INGAAS grown on inp substrates," *Conference Proceedings - International Conference on Indium Phosphide and Related Materials* , 2–5 (2008).

[27] Takagi, T., "Refractive Index of Ga 1- x In x As Prepared by Vapor-Phase Epitaxy," *Japanese Journal of Applied Physics* **17**(10), 1813 (1978).

[28] Wan, Y., Li, Q., Liu, A. Y., Gossard, A. C., Bowers, J. E., Hu, E. L., and Lau, K. M., "Temperature characteristics of epitaxially grown InAs quantum dot micro-disk lasers on silicon for on-chip light sources," *Applied Physics Letters* **109**(1) (2016).

[29] Sánchez, M., Díaz, P., González, G. T. C., Simchez, M., Diaz, P., and Torres, G., "Influence of cavity length and emission wavelength on the characteristic temperature in AlGaAs lasers," **4259** (1995).